

## Velocity structure functions, scaling, and transitions in high-Reynolds-number Couette-Taylor flow

Gregory S. Lewis\* and Harry L. Swinney†

Center for Nonlinear Dynamics and Department of Physics, The University of Texas at Austin, Austin, Texas 78712

(Received 29 June 1998)

Flow between concentric cylinders with a rotating inner cylinder is studied for Reynolds numbers in the range  $2 \times 10^3 < R < 10^6$  (Taylor Reynolds numbers,  $10 < R_\lambda < 290$ ) for a system with radius ratio  $\eta = 0.724$ . Even at the highest Reynolds number studied, the energy spectra do not show power law scaling (i.e., there is no inertial range), and the dissipation length scale is surprisingly large. Nevertheless, the velocity structure functions calculated using extended self-similarity exhibit clear power-law scaling. The structure function exponents  $\zeta_p$  fit Kolmogorov's log-normal model within the experimental uncertainty,  $\zeta_p = (p/3)[1 + (\mu/6)(3-p)]$  (for  $p \leq 10$ ) with  $\mu = 0.27$ . These  $\zeta_p$  values are close to those found in other flows. Measurements of torque scaling are presented that are an order of magnitude more accurate than those previously reported [Lathrop *et al.*, Phys Rev. A **46**, 6390 (1992)]. Measurements of velocity in the fluid core reveal the presence of azimuthal traveling waves up to the highest Reynolds numbers examined. These waves show evidence of a transition at  $R_T = 1.3 \times 10^4$ ; this transition was observed previously in measurements of torque, but our wave velocity and wall shear stress measurements provide the first evidence from local quantities of the transition at  $R_T$ . Velocity measurements indicate that at  $R_T$  there is a change in the coherent structures of the core flow; this is consistent with our analyses of the scaling of the torque. Our measurements were made at two aspect ratios, and no significant dependence on aspect ratio was observable for  $R > R_T$ . [S1063-651X(99)02405-8]

PACS number(s): 47.27.Jv, 47.55.-t, 47.32.-y

### I. INTRODUCTION

The Couette-Taylor system has played an important role in the development of some of the fundamental concepts of fluid dynamics. Most studies of this system have examined instabilities that arise at low to moderate values of the Reynolds number,

$$R = \frac{\Omega a(b-a)}{\nu}, \quad (1)$$

where  $\Omega$  is the inner cylinder angular rotation rate,  $a$  and  $b$  are the inner and outer cylinder radii, and  $\nu$  is the kinematic viscosity. The present study focuses on the behavior near and beyond a transition at  $R_T = 1.3 \times 10^4$ ; beyond this transition the fluid is turbulent and no well-defined transitions have been observed.

Our apparatus was originally designed to determine the Reynolds number dependence of the torque [1]. That experiment was motivated by a prediction for the behavior of the torque at high Reynolds number,

$$G \sim R^\alpha, \quad (2)$$

where  $\alpha = 5/3$  [2,3] and  $G$  is the nondimensional torque,  $G = T/\rho\nu^2L$  ( $T$  is the torque,  $\rho$  is the fluid density, and  $L$  is the length of the inner cylinder). This scaling is analogous to the behavior found for Rayleigh-Bénard convection, where

experiments and theory yield a power law for the dependence of the Nusselt number  $N$  (the dimensionless heat transport) on the Rayleigh number  $R_a$  (the dimensionless temperature difference),  $N \sim R_a^{2/7}$  [4]. The previous experiment on Couette-Taylor turbulence yielded, contrary to expectations, no region of constant exponent  $\alpha$ . The experiment also revealed the transition at  $R_T$ , where there was a marked change in the slope of the exponent  $\alpha$  as a function of  $R$ .

In this paper we present velocity and wall shear stress measurements that provide the first evidence from local quantities of the transition at  $R_T$ . Also, we present torque measurements that are an order of magnitude more precise and accurate than the earlier data [1]. Our results for the velocity spectra and velocity structure functions indicate that Couette-Taylor flow is unlike most other turbulent flows—even at a high Reynolds number,  $R \approx 10^6$ , we observe no inertial range. However, the structure functions computed by extended self-similarity (plotting the  $p$ th-order structure function versus the third-order function) exhibit a power-law scaling region that enables us to obtain precise values for the structure function exponents, and these exponent values are close to those found for other turbulent flows.

The rest of this paper is organized as follows. Section II describes the experimental apparatus and the measurement techniques. Section III presents the results from torque measurements and discusses models of torque scaling. Section IV presents evidence for a transition at  $R_T = 13\,000$ . Section V discusses the Reynolds stress and turbulent intensity and compares the Kolmogorov, Taylor, and dissipation length scales. Section VI presents the scaling exponents of longitudinal structure functions calculated using extended self-similarity. Section VII is a discussion. An Appendix presents

\*Electronic address: lewis@dnai.com

†Electronic address: swinney@chaos.ph.texas.edu

results for probability distribution functions for the wall shear stress and for velocity differences.

## II. EXPERIMENTAL SYSTEM

The experimental system consists of a Couette-Taylor apparatus, drive motor, motor control electronics, temperature regulation system, and a computer for control and data acquisition. The design considerations and apparatus were described in [1]. The description here emphasizes the changes and additions to that original system [5].

### A. The Couette-Taylor system

The Couette-Taylor apparatus has a stationary clear Plexiglas outer cylinder with an inside radius of  $b = 22.085$  cm and a stainless steel inner cylinder with an outer radius of  $a = 15.999$  cm; thus the gap is  $b - a = 6.086$  cm and the radius ratio is  $\eta = a/b = 0.724$ . To reduce end effects the inner cylinder is made in three sections with only the 40.65 cm center section used to measure torque. The total length of the apparatus is  $L = 69.5$  cm, which yields for the aspect ratio  $\Gamma = L/(b - a) = 11.4$ . In some experiments the fluid height was reduced to 60.0 cm ( $\Gamma = 9.8$ ) by the addition of a spacer to the top head. In all cases, both ends of the annulus were stationary.

The end sections of the inner cylinder are rigidly attached to the drive shaft. The center section of the inner cylinder is mounted on low friction bearings and is driven through a strain arm which transmits all of the torque required to turn the center section. The inner cylinder is rotated by a 2 kW motor (PMI model JR25M6CH), which has zero cogging and turns smoothly down to zero rotation frequency. (The motor used in the previous measurements had speed variations due to 12 preferred rotor positions; these speed variations were the dominant feature of wall shear stress measurements on the inner cylinder.) The motor speed is measured by an optical encoder with 2500 pulses per revolution (Dynamics Research Corp 25-031-B16-2500).

We have measured torque for flow states with eight and ten vortices with  $\Gamma = 11.4$ , and for a state with eight vortices with  $\Gamma = 9.8$ . For eight vortices and  $\Gamma = 11.4$ , measurements were made with six different values of the kinematic viscosity ranging from 0.009 68 to 0.208 cm<sup>2</sup>/s. The 0.009 68 cm<sup>2</sup>/s fluid was water; the 0.1521 cm<sup>2</sup>/s fluid was ethylene glycol; the other fluids (0.0229, 0.0403, 0.1148, and 0.208 cm<sup>2</sup>/s) were water-glycerol mixtures. The viscosity was measured with Cannon-Fenske Routine viscometers with an accuracy of  $\pm 0.5\%$ . There was no measurable difference in the torque for the pure and binary fluids, which indicates that errors due to concentration gradients in the mixtures are insignificant.

For the ten-vortex state, measurements were made with water-glycerol mixtures with viscosities of 0.1148 and 0.203 cm<sup>2</sup>/s. For the shorter aspect ratio,  $\Gamma = 9.8$ , measurements were made in the eight-vortex state using five fluids with viscosities ranging from 0.009 68 to 0.208 cm<sup>2</sup>/s.

### B. Temperature measurement and control

Temperature control is important because of the temperature dependence of viscosity. The working fluid temperature

is controlled to within a few millidegrees Kelvin of the set point throughout a torque run, while the power dissipated ranges from about 10 W to 2 kW. Temperature is measured with Thermometrics Fastip thermistors in direct contact with the working fluid. Heat is removed from the system via cooling fluid which is circulated in the top and bottom heads of the apparatus and separated from the working fluid by 1.6 mm thick copper rings.

Since the heat is removed from the ends, we were concerned that axial temperature gradients might cause errors. For Reynolds numbers below about 4000, where the rotation rate is low ( $< 1$  Hz) and the viscosity is high, there were axial temperature variations of up to about 0.05 °C between a thermistor at midheight and another at one-quarter height. For higher Reynolds numbers, where the turbulent transport is much higher, the difference between the two thermistors was less than 0.01 °C.

### C. Flow states

States with different numbers of Taylor vortices can be stable at a given Reynolds number [6]. In our apparatus, we found that if  $R$  was slowly increased from rest, a state with 14 vortices formed at the onset of Taylor vortex flow,  $R_c = 80$ . With further increase in  $R$ , there were transitions to a 12-vortex state at  $R = 2000$ , a ten-vortex state at  $R = 6000$ , and an eight-vortex state at  $R = 20\,000$ ; for  $R > 20\,000$ , only

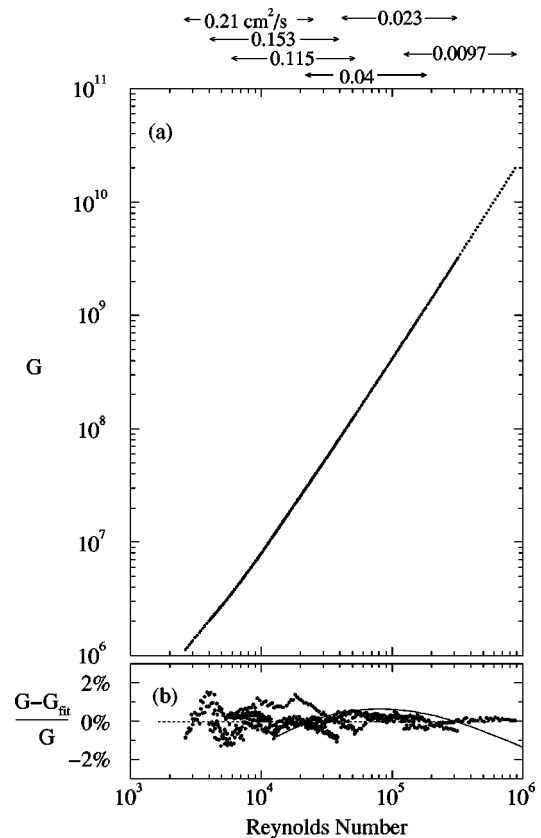


FIG. 1. (a) Experimental values of nondimensional torque in the eight-vortex state for  $\Gamma = 11.4$ ; the average axial wavelength is  $2.86 \times$  the gap width. The viscosities of the fluids used in different runs are indicated at the top. (b) Residuals of fit to Eq. (3). The solid curve is a fit to the Prandtl-von Kármán model (4).

the eight-vortex state was observed. Each of these flow states, once formed, remained stable when  $R$  was slowly decreased to nearly  $R_c$ .

The flow state for large  $R$  was visualized using buoyant particles which go to low pressure regions, making the vortex structure clearly discernible. With this technique we observed, contrary to previous reports [1,7], that vortexlike coherent structures persist with increasing  $R$ , even to  $R = 10^6$ , our highest  $R$  examined. However, for  $R \geq 100\,000$ , the vortex boundaries drifted axially and the number of vortices was not well-defined.

A stable anomalous nine-vortex state was produced at  $R = 1500$  by introducing a convective perturbation. In this state there was an outflow boundary at the bottom end ring. Normally the ends are inflow boundaries due to Ekman pumping—the fluid is slowed by the end rings and forced toward the inner cylinder by conservation of angular momentum. Benjamin studied similar anomalous states at lower Reynolds numbers [8–10].

Our measurements focus on the eight-vortex state because it is stable over the widest Reynolds number range in our apparatus,  $80 \leq R \leq 100\,000$ . For convenience, we will refer to the flow for  $R \geq 100\,000$  as the eight-vortex state, even though the number of vortices is not well defined.

#### D. Torque measurements

Improvements in the system resulted in torque measurements that for a given fluid are reproducible to 0.1% [5], an order of magnitude increase in precision over previous measurements [1]. Torque is measured using a Taedea Huntleigh model 305 7 kg full bridge bending beam strain arm with total error of less than 0.02% full scale. A circuit consisting of a REF-01 voltage reference source and a Darlington transistor provides a 10 V DC excitation signal to the strain arm. The strain gauge signal is amplified ( $\times 500$ ) with an Analog Devices AD624 instrumentation amplifier placed inside the center section of the inner cylinder (this minimizes noise and eliminates the problem of slip ring resistance). The measure-

ment uncertainty is dominated by the hysteresis associated with the seals and the contacts between the strain arm and inner cylinder.

#### E. Velocity and wall shear stress measurements

The wall shear stress is measured with TSI model 1268W hot film probes flush mounted on the outer and inner cylinders. Azimuthal velocity measurements are made with TSI model 1210AJ-20W cylindrical and 1264BV conical hot film probes with TSI 1653B and 1750 anemometers. Anemometer outputs are fed to computer-controlled variable offset and gain instrumentation amplifiers (Burr Brown PGA-202), followed by two computer-controlled, variable frequency, switched capacitor, eighth order Butterworth filters (National Semiconductor MF-4) and active fixed frequency low-pass antialiasing filters.

Velocity was measured in the middle of the gap, 4.35 cm above midheight for  $12\,000 \leq R \leq 5.4 \times 10^5$ . The sampling rate was 2500 times the inner cylinder rotation frequency; 10 to 20 million samples were acquired for each Reynolds number.

For the wall shear stress, 5 million samples were taken from each of the four probes with a sampling rate that varied from 256 times the rotation rate for the  $0.165 \text{ cm}^2/\text{s}$  fluid to 1536 times the rotation rate for the  $0.0091 \text{ cm}^2/\text{s}$  fluid.

As an additional check and to provide absolute measurements of the azimuthal component of the velocity, a 0.3-cm-diam Pitot tube (United Sensor PCC-12-KL) was used in measurements as a function of radial position (at annulus midheight). The Pitot tube was adjusted to be tangential to the flow.

### III. TORQUE MEASUREMENTS AND THE PRANDTL-VON KÁRMÁN SKIN FRICTION LAW

#### A. Torque measurements

Measurements of torque as a function of Reynolds number for the eight-vortex state are presented in Fig. 1(a). A cubic least squares fit of these data yields

$$\log_{10} G = \begin{cases} 0.2005(\log_{10} R)^3 - 1.970(\log_{10} R)^2 + 7.775(\log_{10} R) - 5.516, & 2600 \leq R \leq 13\,000, \\ -0.006360(\log_{10} R)^3 + 0.1349(\log_{10} R)^2 + 0.8850(\log_{10} R) + 1.610, & 13\,000 \leq R \leq 10^6, \end{cases} \quad (3)$$

which is accurate above  $R = 13\,000$  to 0.5% rms, and to 0.6% rms for lower  $R$ . The residuals of this fit are shown in Fig. 1(b). Most of the variations shown in Fig. 1(b) arise from the  $\pm 0.5\%$  uncertainty in the viscosity measurements.

We examined the dependence of the torque on the axial wavelength by comparing measurements for the eight- and ten-vortex states, as shown in Fig. 2(a). For  $R < 13\,000$ , the torque scaling and velocity spectra indicate different dynamics for the eight- and ten-vortex states. For larger  $R$ , the torque values for the two states are within 2%.

The dependence of torque on aspect ratio was examined by comparing measurements on the shortened system ( $\Gamma = 9.8$ ) with those on the full height system ( $\Gamma = 11.4$ ), as shown in Fig. 2(b). The torque values for the two aspect

ratios differ less than 1% for  $10^4 < R < 10^5$ , but the difference increases to 4% at  $10^6$ . Presumably this increasing difference is a consequence of Ekman pumping, which causes the size of the end vortices to increase with increasing  $R$ . The larger end vortices are ‘‘felt’’ by the measurement section of the inner cylinder more strongly with the short aspect ratio, resulting in a larger measured torque for this case.

#### B. Torque scaling

For power-law scaling, the exponent in Eq. (2) would be constant with a value given by  $\alpha = d(\log_{10} G)/d(\log_{10} R)$ , which is the slope of Fig. 1(a). This slope was approximated by taking a sliding linear least-squares fit for each fluid sepa-

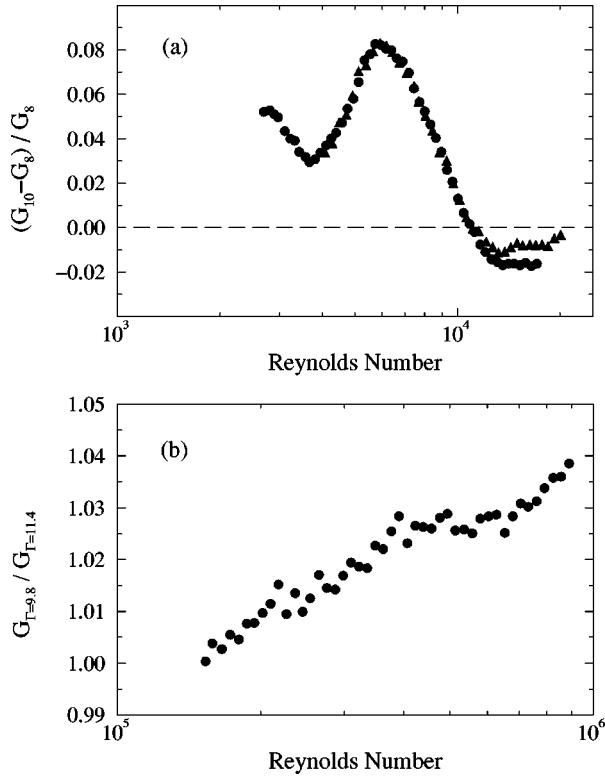


FIG. 2. (a) Comparison of torque in the eight- and ten-vortex states ( $\Gamma = 11.4$ ), which have average wavelengths, respectively, of 2.28 and 2.86 times the gap width.  $G_{10}$  was taken directly from measurements for viscosities of  $0.11 \text{ cm}^2/\text{s}$  ( $\blacktriangle$ ) and  $0.22 \text{ cm}^2/\text{s}$  ( $\bullet$ ). The values of  $G_8$  were calculated using a linear regression of  $\log_{10} R$  versus  $\log_{10} G$  for all the eight-vortex data within an interval of  $\Delta(\log_{10} R) = 0.12$  centered at the corresponding ten-vortex data point. (b) Ratio of torques measured for the eight-vortex state at aspect ratios of 9.8 and 11.4, which have average wavelength, respectively, of 2.46 and 2.86 times the gap width.

rately over a range of  $\Delta(\log_{10} R) = 0.1$ , and the results are shown in Fig. 3(a). Clearly there is no region where  $\alpha$  is constant. Thus we find no power-law scaling, which is in accord with the observations of Lathrop *et al.* [1]. The transition in the behavior of  $\alpha$  at approximately  $R_T = 1.3 \times 10^4$  will be discussed in Sec. IV.

Figure 3(b) compares the scaling exponent for the ten-vortex state with  $\Gamma = 11.4$  and the eight-vortex state with both  $\Gamma = 9.8$  and  $11.4$ . Although the torque scaling depends on the fluid state below the transition at  $R_T$ , for larger  $R$  the values of  $\alpha$  for the different states are in good accord.

### C. Comparison with Prandtl–von Kármán skin friction law

Lathrop *et al.* [1] and Panton [11] have shown that a prediction for the scaling behavior of the torque above  $R_T$  can be obtained by assuming logarithmic boundary layers at each cylinder wall. Lathrop *et al.* treated the core region as an extension of the boundary layers, while Panton assumed constant angular momentum in the core region. The assumption of logarithmic boundary layers with a core of approximately constant angular momentum is supported by measurements by Smith and Townsend [7]. Lathrop *et al.* and Panton both arrived at the following relation between torque and Reynolds number:

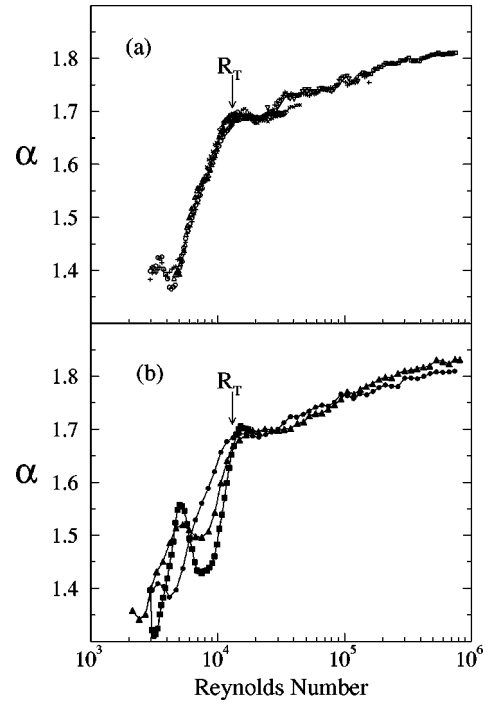


FIG. 3. (a) Local exponents for the torque data of Fig. 1:  $\alpha = d(\log_{10} G)/d(\log_{10} R)$  calculated for each fluid separately, using a sliding least-squares fit over the interval  $\Delta(\log_{10} R) = 0.1$  (eight-vortex state,  $\Gamma = 11.4$ ). (b) Comparison of torque exponents for the eight-vortex state with  $\Gamma = 9.8$  ( $\blacktriangle$ ) and  $\Gamma = 11.4$  ( $\bullet$ ), and for the ten-vortex state with  $\Gamma = 11.4$  ( $\blacksquare$ ). For each state the slopes from all fluids are averaged into bins of  $\Delta(\log_{10} R) = 0.05$ .

$$\frac{R}{\sqrt{G}} = N \log_{10} \sqrt{G} + M, \quad (4)$$

where, for the two models,  $N$  and  $M$  are different functions of the von Kármán constant and the geometry. By defining the skin friction coefficient,  $C_f = G/R^2$ , we obtain from Eq. (4) the Prandtl–von Kármán skin friction law:

$$\frac{1}{\sqrt{C_f}} = N \log_{10} R \sqrt{C_f} + M. \quad (5)$$

The torque data fit (5) remarkably well, as Fig. 4(a) demonstrates. The parameter values from the fit are  $N = 1.56$  and  $M = -1.83$ , which for Panton's model imply a von Kármán constant of  $\kappa = 0.44$ , close to the standard value of 0.40 [12].

Equations (2) and (4) can be solved to obtain a relation for the Reynolds number dependence of the scaling exponent  $\alpha$ ,

$$\alpha = \frac{2}{1 + \frac{2 \log_{10} e}{\log_{10} G + \frac{2M}{N}}}. \quad (6)$$

This prediction is compared with our measurements in Fig. 4(b). The agreement of the torque measurements with Eq. (6) is much better than that reported in [1].

To test the assumption that the angular momentum is constant in the core of the flow, we made the measurements

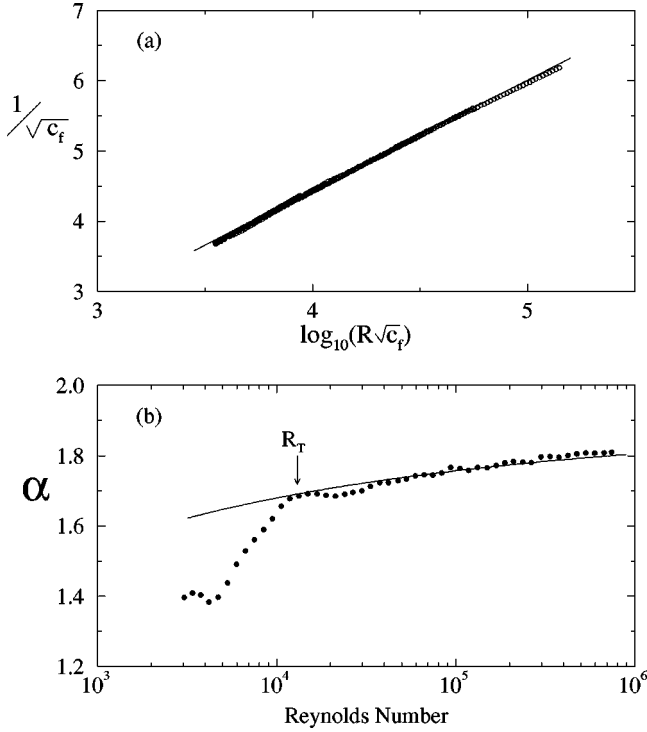


FIG. 4. (a) Comparison of a Prandtl–von Kármán skin friction law (5) with the experimental data ( $\circ$ ). (b) Comparison of scaling exponent from experimental data ( $\bullet$ ) with fit to Eq. (6) (solid line). In both graphs fit parameters were  $M = -1.81$  and  $N = 1.56$ , corresponding to a von Kármán constant of  $\kappa = 0.44$ .

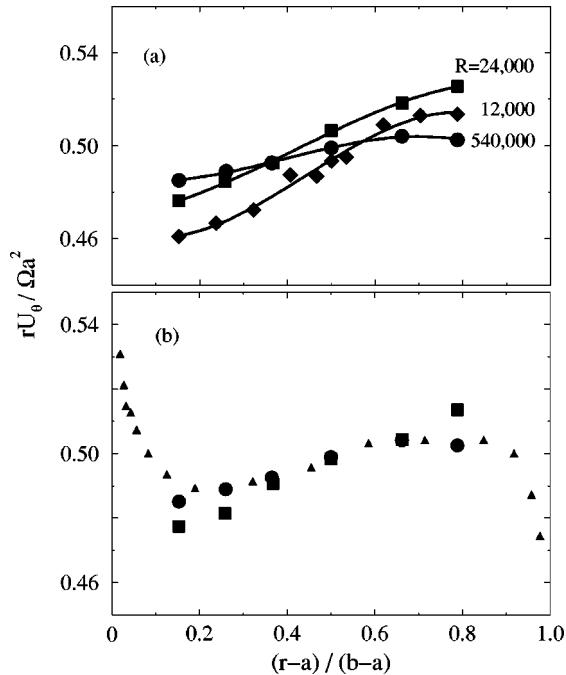


FIG. 5. (a) Specific angular momentum at cylinder midheight (an inflow boundary) as a function of radius. (b) Comparison of present data ( $\eta=0.724$ ) for  $R=50\,000$  ( $\blacksquare$ ) and  $R=540\,000$  ( $\bullet$ ) with data of Smith and Townsend ( $\eta=2/3$ ) for  $R=50\,000$  ( $\blacktriangle$ ).

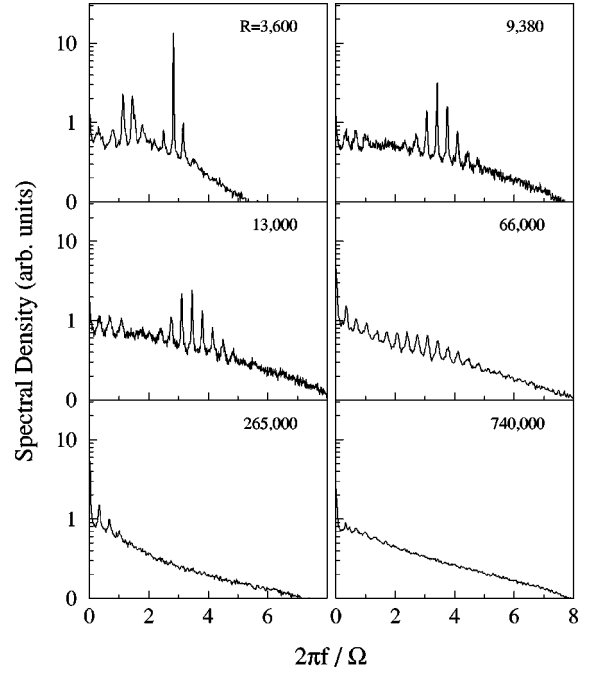


FIG. 6. Velocity power spectra for state with eight vortices, showing the presence of azimuthal traveling waves; all peaks are close multiples of the lowest frequency peak. Each data set contains at least  $5 \times 10^5$  points sampled 40 times per inner cylinder revolution. Measurements were made at a vortex center: midgap ( $r=19$  cm) and one-half vortex above midheight of the cylinder.

shown in Fig. 5. There is a small increase in specific angular momentum with radius in both our experiments and those of Smith and Townsend [13], but to good approximation it is constant and given by

$$\frac{U_\theta r}{\Omega a^2} \approx \frac{1}{2}. \quad (7)$$

#### IV. TRANSITION AT $R_T=13\,000$

The measurements of torque, a globally averaged property of the flow, reveal a transition at  $R_T=13\,000$ , where there is a sharp change in the slope of the torque exponent (Fig. 3). Although the transition at  $R_T$  can be explained as arising from the development of logarithmic boundary layer profiles [1,11], there must also be changes in the structure of the core region, where the torque is transmitted by the Reynolds stress (cf. Sec. V B). We now examine velocity measurements in the core to search for evidence for the transition at  $R_T$ .

##### A. Azimuthal traveling waves

Azimuthal velocity power spectra obtained on the outflow boundaries and within a vortex reveal peaks at integer multiples of a fundamental frequency (Fig. 6). Cross correlation of velocity measurements with two probes at the same radius and height but separated by  $5.5^\circ$  azimuthally show that the spectral peaks correspond to azimuthal traveling waves. (The peaks are weak or absent on the inflow boundaries.) At low Reynolds numbers there is a dominant peak, but as the transition is approached with increasing  $R$ , more modes rapidly

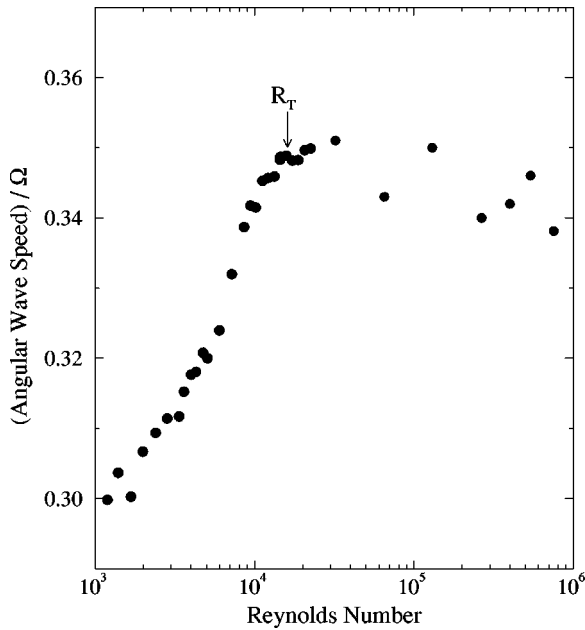


FIG. 7. Angular velocity of azimuthal traveling waves for the eight-vortex state. The angular wave speed was calculated by dividing the frequencies of the dominant peaks by the mode number and averaging the results for each Reynolds number.

become excited and the peaks become weaker and comparable in amplitude. For  $R > R_T$ , the peaks gradually decrease in amplitude, but the lowest frequency peak remains discernible in spectra up to at least  $R = 750\,000$ , even though the Taylor vortices are no longer stationary.

Measurements of the wave speed as a function of Reynolds number indicate a change in the behavior of the fluid core at  $R_T$  (Fig. 7): the wave speed increases monotonically below  $R_T$  and then becomes approximately constant above  $R_T$ . The wave speed value at  $R_T$ , 0.35, is the same as the normalized angular fluid velocity,  $U_\theta/r\Omega$ , computed from Eq. (7) at midgap.

### B. Wall shear stress correlations

The azimuthal traveling waves are also visible in wall shear stress measurements on both the outer and inner cylinders. The same frequencies are measured by the wall shear stress probes as in the velocity spectra, except that the peaks in the wall shear stress spectra are much weaker, and the frequencies measured at the inner cylinder are shifted because the sensor is in a moving reference frame. Figure 8 shows cross correlation of measurements by two wall shear stress probes on the outer cylinder. Although the correlation is small, the waves are clearly present at the lower Reynolds numbers, and the amplitude rapidly decreases as the transition is approached.

Cross correlation of wall shear stress measurements with different probes provides further evidence for a transition at  $R_T$ : the maximum correlation coefficient decreases more rapidly above the transition than below it [Fig. 9(a)].

Evidence of the transition at  $R_T$  is also provided by advection velocity values deduced from the wall shear stress measurements: the velocity is calculated by dividing the distance between probes by the time to the maximum correla-

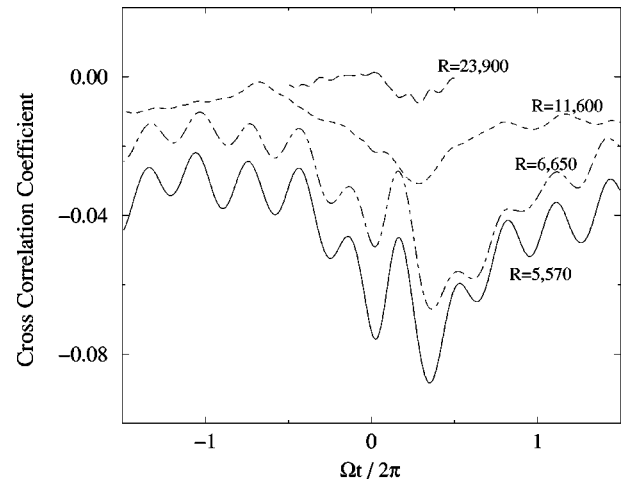


FIG. 8. Wall shear stress cross-correlation measurements showing the presence of azimuthal traveling waves with decreasing amplitude with increasing  $R$ . The two probes are separated both azimuthally and axially on the outer cylinder. One is at midheight, and the second is  $2.75^\circ$  downstream (1.06 cm) and a half vortex (4.35 cm) above the first.

tion [Fig. 9(b)]. The advection velocity increases below the transition but is approximately constant above it. For  $R > R_T$ , the structures that contribute most to the wall shear stress are advected at about 70% of the fluid velocity in the core.

Our final piece of evidence for the transition at  $R_T$  is given by measurements of the decay time,  $t_d$ , of the autocorrelation function of wall shear stress (Fig. 10). [ $t_d$  is calculated by fitting the wall shear stress autocorrelation function to  $A(t) \sim e^{-t/t_d}$ .] For  $R < R_T$ , probes at midvortex show a different decay time behavior from probes at the inflow

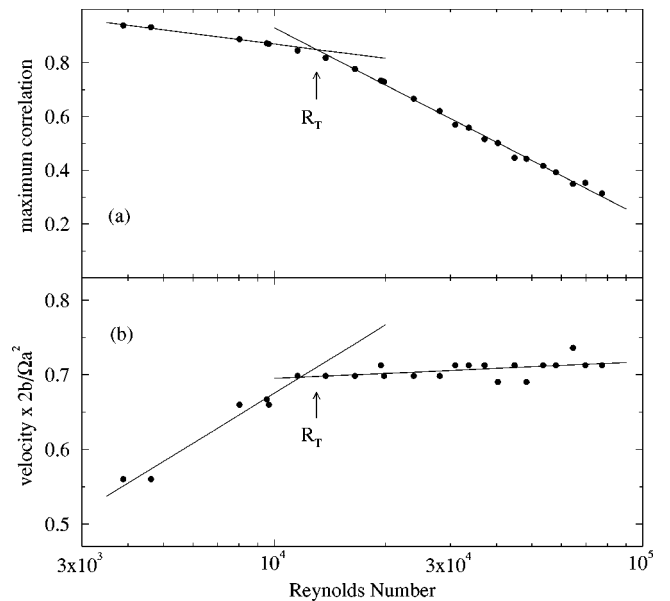


FIG. 9. (a) Maximum of the correlation between wall shear stress probes on the outer cylinder at midheight, separated azimuthally by  $2.75^\circ$  (1.06 cm). (b) Dimensionless advection velocity calculated from time to maximum correlation and the distance between probes. The velocity is normalized by the “core velocity,” the velocity at which the angular momentum  $\Omega a^2 = 1/2$ .

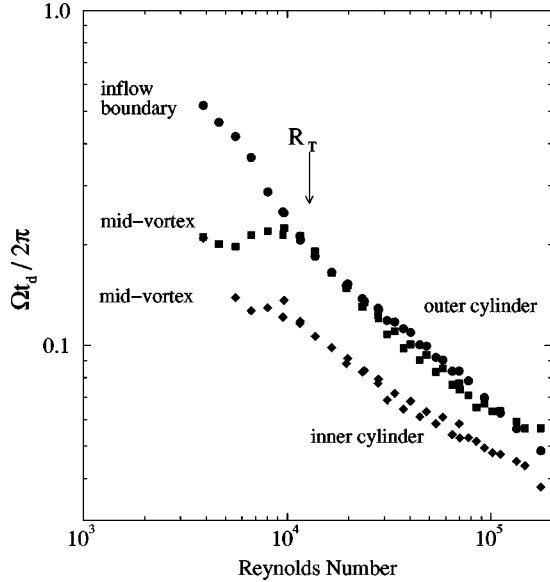


FIG. 10. Decay times calculated from the autocorrelation functions of wall shear stress data.

boundary, but for  $R > R_T$ , all probes show a similar power-law decrease in  $t_d$  with increasing  $R$ .

## V. LENGTH SCALES: DISSIPATION, TAYLOR, AND KOLMOGOROV

### A. Absence of an inertial range

Velocity power spectra at two Reynolds numbers are presented in Fig. 11(a). The abscissa at the top of the figure shows that the length scales are surprisingly large for such high Reynolds numbers. The gap width, 6 cm, is only between 30 and 100 times larger than the smallest length scale above the noise floor.

Figure 11(b) shows that the slopes of the power spectra are not constant over any range in frequency. Thus there is no inertial range, and this flow is fundamentally different from fully developed isotropic turbulence and from turbulent pipe or channel flow, where an inertial range exists and Kolmogorov's  $-5/3$  law holds at much lower Reynolds numbers.

### B. Turbulent intensity, Reynolds stress, and length scales

The azimuthal turbulent intensity,  $i_\theta = \sqrt{\langle u_\theta^2 \rangle} / U_\theta$ , was measured at midgap with the hot film probes to be 6.0–7.5%, with the lower value at higher Reynolds numbers. A fit above  $R_T$  yields

$$i_\theta = 0.10R^{-0.125}. \quad (8)$$

The radial turbulent intensity for  $10\,000 < R < 60\,000$  at an inflow boundary was measured by ultrasound to be about 12%. These turbulent intensities are similar to those reported in [7].

The torque per unit length is transmitted by the Reynolds stress and viscous forces:

$$\frac{T}{L} = \frac{\nu^2 G}{2\pi} = \langle u_r u_\theta \rangle r^2 - \nu r^3 \frac{d}{dr} \left( \frac{U_\theta}{r} \right). \quad (9)$$

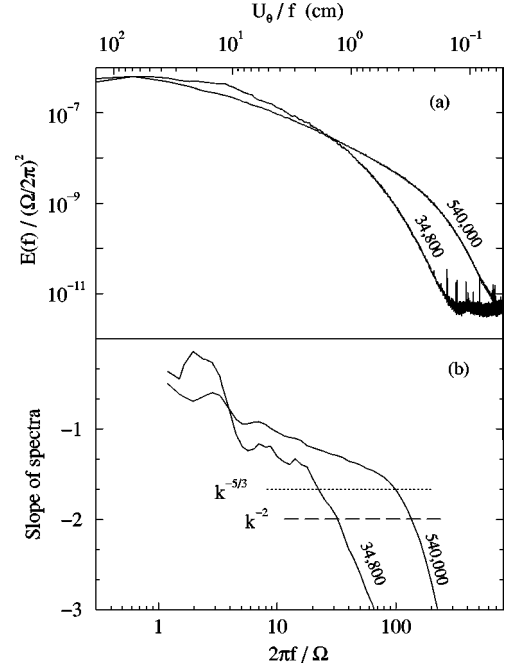


FIG. 11. (a) Power spectra of azimuthal velocity measured in the core region. ( $R=540\,000$  and  $R=34\,800$  correspond to  $R_\lambda=270$  and  $R_\lambda=80$ , respectively.) (b) Slopes of the same spectra. The slopes were calculated by performing a sliding linear least-squares fit of the spectra over a range of  $\Delta(\log_{10} R)=0.05$ . The dashed line at  $-2$  indicates maximum dissipation. The dotted line indicates where the slope is equal to  $-5/3$ , the Kolmogorov exponent value. The lack of a region of constant slope equal to  $-5/3$  shows that there is no inertial range.

The torque data and Eq. (7) show that in the core, the viscous contribution decreases from about 2% of the total at  $R=10^4$  to about 0.06% at  $R=10^6$ .

We now compare dissipation calculated from the velocity data and from the torque. From the hot film data, the dissipation (assuming isotropy) is given by

$$\epsilon = 15\nu \langle (\partial u / \partial x)^2 \rangle = 15\nu \int k^2 E(k) dk, \quad (10)$$

where  $x$  and  $u$  are the streamwise direction and velocity (we treat the local velocity fluctuations in Cartesian rather than cylindrical coordinates). From the torque the average dissipation per unit mass is given by the total power input  $T\Omega$  divided by the mass of the fluid:

$$\langle \epsilon \rangle = \frac{\nu^2 G \Omega}{2\pi(b^2 - a^2)}. \quad (11)$$

The dissipation calculated from the power spectra, Eq. (10), is between 30% and 50% of that calculated from the torque, Eq. (11), with the largest discrepancy at low  $R$ ; this is within the expected range and in the expected direction, considering the anisotropy and that the dissipation from the torque includes the boundary layers while the dissipation from the hot film data is point measurement in the core [14].

The Kolmogorov scale is

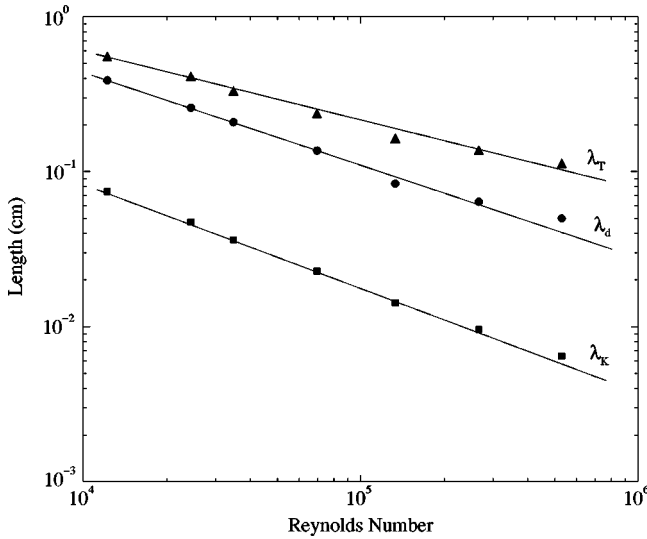


FIG. 12. Length scales: ( $\blacktriangle$ )  $\lambda_T$ , Taylor microscale calculated from Eq. (13); fit is  $\lambda_T = 47.0R^{-0.473}$ . ( $\bullet$ )  $\lambda_d$ , length at the maximum dissipation in the velocity power spectra; fit is  $\lambda_d = 115R^{-0.605}$ . ( $\blacksquare$ )  $\lambda_K$ , Kolmogorov length scale calculated from Eqs. (10) and (12); fit is  $\lambda_K = 42.0R^{-0.674}$ .

$$\lambda_K = \left[ \frac{\nu^3}{\epsilon} \right]^{1/4}, \quad (12)$$

where we use Eq. (10) to determine  $\epsilon$ . The Taylor microscale is defined as [15]

$$\lambda_T^2 = \frac{\langle u^2 \rangle}{\langle (\partial u / \partial x)^2 \rangle} = \frac{\int E(k) dk}{\int k^2 E(k) dk}. \quad (13)$$

Figure 12 shows  $\lambda_K$  and  $\lambda_T$  determined from Eqs. (12) and (13). These values of  $\lambda_T$  were used to calculate the Taylor Reynolds numbers,  $R_\lambda = \langle u^2 \rangle \lambda_T / \nu$ , given in this paper. Below  $R = R_T$ ,  $R_\lambda$  was extrapolated and is less accurate.

The dissipation is greatest at the wave number  $k_d$ , which maximizes the integrand of Eq. (10). From this we define a dissipation length scale  $\lambda_d = 1/k_d$ .

The Kolmogorov, Taylor, and dissipation length scales are shown in Fig. 12.  $\lambda_d$  is about seven times larger than  $\lambda_K$ , close to the nine times found for fully developed turbulence [16]. The Taylor scale is about twice as large as the dissipation scale, indicating that we do not have the separation of scales required for the development of an inertial range.

## VI. VELOCITY STRUCTURE FUNCTION SCALING

The longitudinal velocity structure functions are defined as

$$\langle (\Delta u_s)^p \rangle \equiv \langle [u(x+s) - u(x)]^p \rangle, \quad (14)$$

where  $u(x)$  is the velocity component at the position  $x$  parallel to the relative displacement  $s$ . These were calculated using Taylor's hypothesis:  $u(x+s, t) = u(x, t-s/U)$ . The structure functions measure increasingly rare events as  $p$  in-

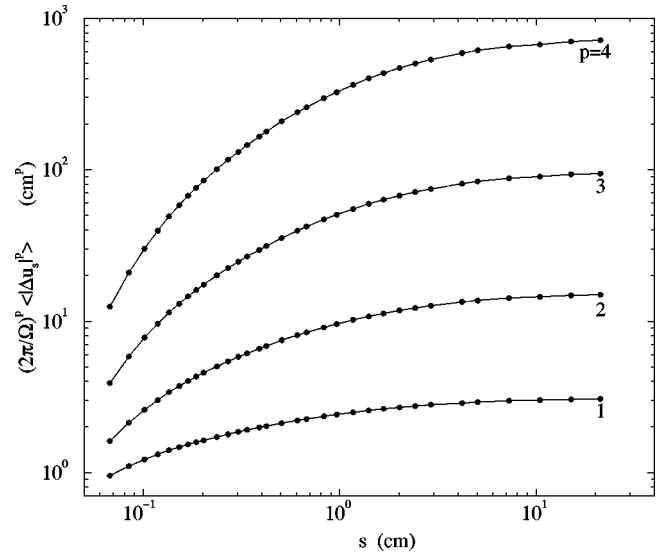


FIG. 13. Velocity structure functions at  $R = 540\,000$ . The velocity in units of cm/s was normalized by the inner cylinder rotation frequency (Hz).

creases. For fully developed turbulence these are believed to scale as power laws of  $s$  [17]:

$$\langle (\Delta u_s)^p \rangle \sim s^{\zeta_p}. \quad (15)$$

Deviations from the Kolmogorov 1941 values of  $\zeta_p = p/3$  [18] characterize the intermittent nature of the flow. The first four structure functions are shown in Fig. 13. We use the absolute values of the velocity differences in calculating the structure functions because this is more statistically stable. While there is no theoretical justification for this, numerical and experimental evidence suggests that using the absolute values does not significantly change the exponent in Eq. (15) [19–22].

Like the power spectra, the structure functions show no region of power-law scaling. However, Benzi *et al.* [19] have shown that the range of power-law behavior can be extended to lower Reynolds numbers using extended self-similarity (ESS), that is, by plotting  $\langle |\Delta u_s|^p \rangle$  versus  $\langle |\Delta u_s|^3 \rangle$  on a log-log plot; the slope is then  $\zeta_p / \zeta_3$ , and  $\zeta_p$  is determined by taking  $\zeta_3 = 1$  from Kolmogorov's 4/5 law. Figure 14 shows the structure functions using extended self-similarity for  $p = 1$  to  $p = 10$ . These are remarkably linear even though we clearly do not have anything resembling a scaling region in the energy spectra or in the classical structure function plots, and the length scales in the core are surprisingly large. The structure functions of other flows show deviations from a straight line at five to twenty times the Kolmogorov microscale, while the data of the present study are linear over the full range of length scales: from  $s = 0.07$  cm, which is just above the noise floor, to  $s = 42$  cm where the velocity differences are Gaussian. (For discussions of the range of length scales at which ESS applies, see [21–25].)

The  $\zeta_p$ 's at  $R = 69\,000$  and  $R = 540\,000$  are compared to those obtained by others in Table I [19,23–26]. The values for  $\zeta_p$  in Table I agree quite well up to  $p = 6$ . Some of the discrepancy above  $p = 6$  is due to less reliable statistics and some due to differences in the method of calculating  $\zeta_p$ . A

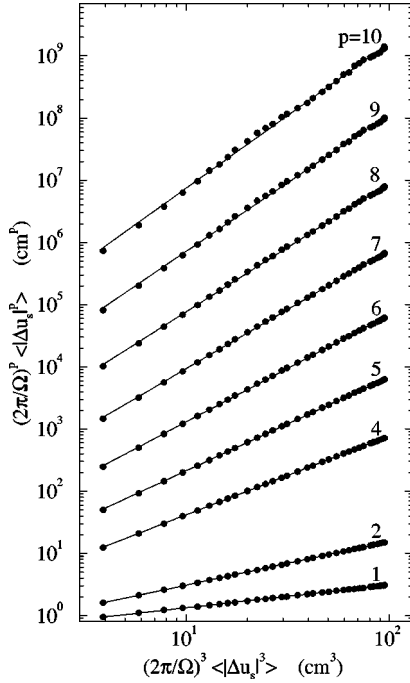


FIG. 14. Evidence for extended self-similarity: third versus first through tenth order velocity structure functions at  $R = 540\,000$ . Lines are linear least-squares fits with slopes given in Table I. The velocity was normalized by the inner cylinder rotation frequency (Hz). For the points shown above,  $s$  varies between 0.067 cm and 42.2 cm, corresponding to normalized frequencies ( $2\pi f/\Omega$ ) of 625 and 1, respectively (see Fig. 11).

comparison of different methods of calculating  $\zeta_p$  can be found in [23] and a discussion of the values of  $\zeta_p$  can be found in [17] and in [22].

In Fig. 15 we compare our measurements of  $\zeta_p$  with the predictions of two theories [17]: (a) Kolmogorov's log-normal model,

$$\zeta_p = \frac{p}{3} \left( 1 + \frac{\mu}{6} (3-p) \right), \quad (16)$$

TABLE I. Values of  $\zeta_p$  calculated using extended self-similarity compared with values measured by others.

$p$	$R = 69\,000^a$	$R = 540\,000^b$	Anselmet <sup>c</sup> [26]	Benzi <sup>d</sup> [19]	Stolovitzky <sup>e</sup> [25]	Belin <sup>d</sup> [24]	Boratav <sup>f</sup> [23]
1	0.37	0.37				0.4	
2	0.70	0.70	0.71	0.71	0.70	0.70	0.69
3	1	1	1	1	1	1	1
4	1.27	1.27	1.33	1.28	1.20	1.26	1.28
5	1.51	1.50	1.54–1.65	1.53	1.52	1.50	
6	1.72	1.72	1.8	1.78	1.62	1.71	1.78
7	1.92	1.90	2.06–2.12	2.01	1.96	1.90	
8	2.09	2.06	2.22–2.28	2.22	2.00	2.08	2.21
9	2.26	2.19	2.41–2.52		2.36	2.19	
10	2.41	2.32	2.6	2.60	2.36	2.30	2.60

<sup>a</sup> $R_\lambda = 80$ .

<sup>b</sup> $R_\lambda = 270$ .

<sup>c</sup>Direct calculation on experimental data. Range of numbers is for different experiments.

<sup>d</sup>Extended self-similarity on experimental data.

<sup>e</sup>Experimental data fit to functional form.

<sup>f</sup>Extended self-similarity on simulation. See [23] for values of  $\zeta_p$  using other methods.

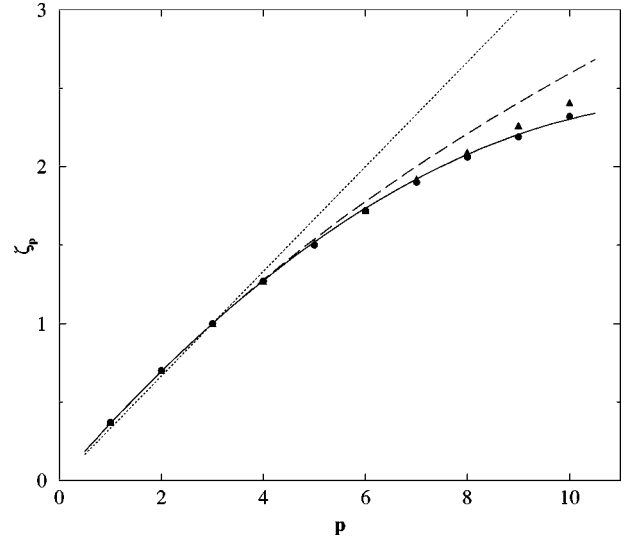


FIG. 15. Comparison of the values of the structure function exponents  $\zeta_p$  determined from the present experiments at  $R = 69\,000$  ( $\blacktriangle$ ) and  $R = 540\,000$  ( $\bullet$ ) with predictions of the log-normal (16) (solid line) and She-Lévêque (17) (dashed line) models. In the absence of intermittency, Kolmogorov theory [18] gives  $\zeta_p = p/3$  (dotted line).

where  $\mu$ , the exponent for the second moment of the dissipation, has the value 0.27 for the best fit to our data; and (b) She and Lévêque's result obtained assuming a hierarchy of fluctuation structures associated with vortex filaments [27],

$$\zeta_p = \frac{p}{9} + 2 - 2(2/3)^{p/3}, \quad (17)$$

which has no adjustable parameters. Although the log-normal model provides a slightly better fit to our data, this model is known [17] to have two deficiencies: it violates the Novikov inequality and it implies supersonic velocities at very high Reynolds number.

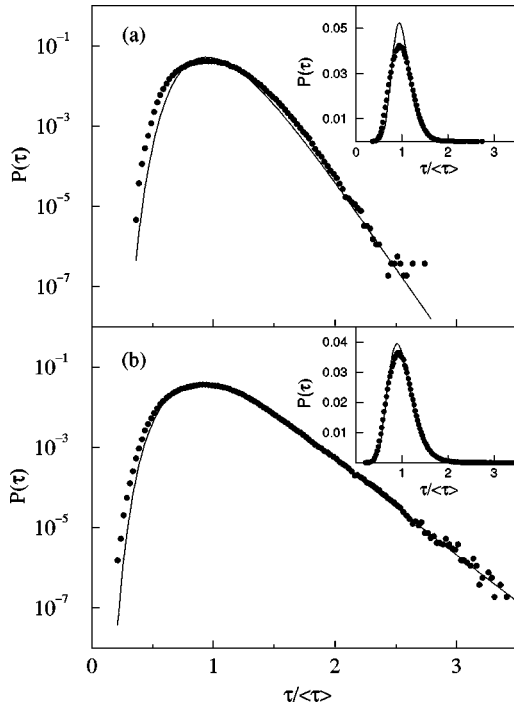


FIG. 16. Comparison of log-normal distribution with observed wall shear stress measurements at  $R=70300$ : (a) inner wall, (b) outer wall. Insets show the same data with a linear ordinate.

## VII. DISCUSSION

We have found that even at  $R=10^6$  ( $R_\lambda=290$ ), Couette-Taylor flow exhibits no inertial range and the dissipation scale is large [about 3% of  $(b-a)/2\pi$ ]. In contrast, pipe and channel flow exhibit a well developed inertial range at such high  $R$ . Perhaps the rotation suppresses the energy cascade in the Couette-Taylor system. A clearly defined inertial range should emerge in our system when  $\lambda_T \gg \lambda_d$ , which probably corresponds to  $R > 10^8$  (Fig. 12); because of the Joule heating, such high Reynolds numbers could not be achieved in a table top apparatus unless the working fluid were helium at low temperatures.

Despite the large length scales and the absence of an inertial range, we were able to obtain, using extended self-similarity, the scaling exponents  $\zeta_p$  for the longitudinal velocity structure function. Our values for  $\zeta_p$  are slightly lower than those measured in most other turbulent flows; however, they agree well with those measured by Belin *et al.* [24]. Although the lower values may not be significant, they may suggest that Couette-Taylor flow is more intermittent, but to test this supposition, we would have to consider the transverse structure functions. (For transverse structure functions the displacement is perpendicular to the velocity component and the deviations from Kolmogorov 1941 theory are even larger [23,28].)

We have presented very precise torque measurements that yield a scaling exponent  $\alpha$  for the dimensionless torque,  $G \sim R^\alpha$ , which is not constant but increases linearly with  $\log_{10} R$  for  $R > R_T$  (Fig. 3). However,  $\alpha$  cannot increase without limit—there is a rigorous upper bound,  $\alpha=2$ , which has been derived from the Navier-Stokes equation [29]; intermittency could lead to a smaller asymptotic value for  $\alpha$ . Ex-

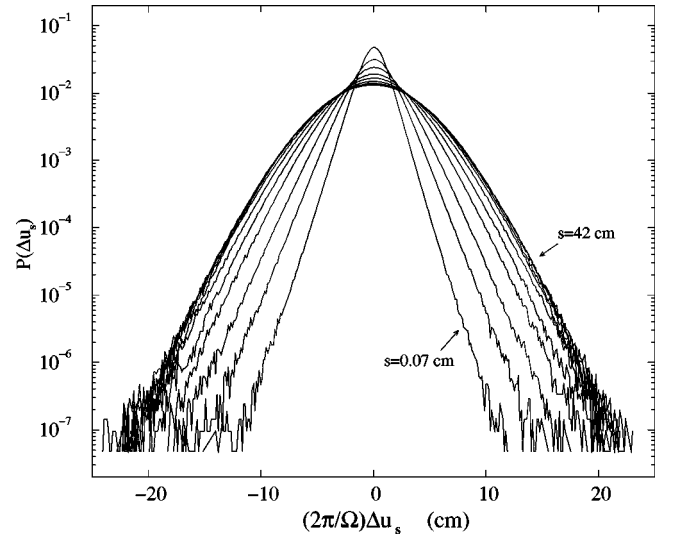


FIG. 17. Probability distribution functions of velocity increments at  $R=540000$ . Distributions change from having exponential tails to Gaussian as the separation distance  $s$  is increased in steps of approximately a factor of 2 from 0.07 cm to 42 cm.

trapolating our results for  $\alpha$  yields an estimate of the value of  $R$  when  $\alpha=2$ :  $R \approx 3 \times 10^8$ , which is comparable to our estimate for  $R$  for the emergence of an inertial range.

We have presented evidence from local measurements for the transition at  $R_T=13000$ , which was first observed in measurements of torque, a global quantity [1]; this transition is clearly evident in our results for torque exponent (Fig. 3). The transition is also clearly discernible in local velocity measurements of the azimuthal wave speed (Fig. 7) and also in the amplitude of the waves detected in wall shear stress data (Fig. 8). Further, this transition can be seen in the advection velocity determined from cross correlation of signals from two wall shear stress probes [Fig. 9(b)]. Finally, the wall shear stress measurements show a greater axial variation below  $R_T$  than above  $R_T$  (Fig. 10).

## ACKNOWLEDGMENTS

We acknowledge the help and inspiration of our colleague, David J. Tritton, who died last year. He will be greatly missed. We thank everyone who worked on this experiment, especially Paul Umbanhowar (who made the ultrasound measurements), Francisco Melo, and William Manor. Dan Lathrop originally designed and built the experimental apparatus and provided help and guidance for the early part of this project. This project also benefited from discussions with D. Bogard, J. Fineberg, P. S. Marcus, W. D. McCormick, and R. Panton. This work was supported by ONR Grant No. N0014-980-1-0047.

## APPENDIX: PROBABILITY DISTRIBUTIONS OF WALL SHEAR STRESS AND VELOCITY DIFFERENCES

Probability distribution functions are not the subject of this paper, but we present results for the distribution functions here because of their importance in turbulence theory. Above the transition at  $R_T$ , the probability distribution func-

tions of the wall shear stress measured at both the outer and inner cylinders are approximately log-normal, particularly in the tails (Fig. 16). The log-normal distribution has the form

$$P(\tau) = \frac{1}{2\Lambda e^\Delta \sqrt{\Delta} \pi} \exp\left(-\frac{[\ln(\tau/\Lambda)]^2}{4\Delta}\right),$$

where  $\Lambda$  is the most probable value,  $\langle \tau \rangle = \Lambda e^{3\Delta}$  is the mean, and  $\sigma_\tau = \langle \tau \rangle (e^{2\Delta} - 1)^{1/2}$  is the standard deviation. The outer cylinder measurements show more high energy events and are closer to a true log-normal distribution. Energy dissipation at the wall is proportional to the wall shear stress

squared. Since the functional form of this distribution is unchanged by squaring, the dissipation at the wall is also log-normal.

Probability distribution functions for velocity differences (Fig. 17) were calculated using Taylor's hypothesis. From a theoretical perspective the distribution of velocity differences is more important than the distribution of velocities. Figure 17 shows that as the separation distance increases, the distributions change from having exponential tails to Gaussian tails. This contrasts with turbulent flows with a well-developed inertial range, where the distribution functions have been found to have stretched exponential tails [25,30].

- 
- [1] D. P. Lathrop, J. Fineberg, and H. L. Swinney, *Phys. Rev. A* **46**, 6390 (1992).
- [2] A. Barcilon and J. Brindley, *J. Fluid Mech.* **143**, 429 (1984).
- [3] G. P. King, Y. Li, W. Lee, H. L. Swinney, and P. S. Marcus, *J. Fluid Mech.* **141**, 365 (1984).
- [4] B. Castaing, G. Gunaratne, F. Heslot, L. Kadanoff, A. Libchaber, S. Thomae, X.-Z. Wu, S. Zaleski, and G. Zanetti, *J. Fluid Mech.* **204**, 1 (1989).
- [5] G. S. Lewis, Ph.D. dissertation, University of Texas at Austin (1996).
- [6] D. Coles, *J. Fluid Mech.* **21**, 385 (1965).
- [7] G. P. Smith and A. A. Townsend, *J. Fluid Mech.* **123**, 187 (1982).
- [8] T. B. Benjamin, *Proc. R. Soc. London, Ser. A* **359**, 27 (1978).
- [9] T. B. Benjamin and T. Mullin, *Proc. R. Soc. London, Ser. A* **377**, 221 (1981).
- [10] T. B. Benjamin and T. Mullin, *J. Fluid Mech.* **121**, 219 (1982).
- [11] R. L. Panton, *C. R. Acad. Sci., Ser. II* **315**, 1467 (1992).
- [12] The definitions of  $M$  and  $N$  in [1] yield  $\kappa = 0.386$ ; however, the model in [1] also implies that the viscous sublayer matches the logarithmic region at  $y^+ = yu^*/\nu \approx 3$  (where  $u^* = \sqrt{\tau/\rho}$ ) rather than at  $y^+ \approx 11$ . This would imply essentially no viscous sublayer. (Neither [11] nor [7] specify the value of  $y^+$  at which the viscous sublayer matches the logarithmic region.) Variations on these models produce similar values for  $\kappa$  and fits to the data that are almost as good as Eq. (4). For example, using the model of the velocity profile described in the appendix of [7],  $\kappa = 0.396$ .
- [13] From considerations of bounds on solutions to the Navier-Stokes equation, Busse derived an expression for the angular momentum in the limit of infinite Reynolds number [F.H. Busse, in *Statistical Models and Turbulence*, Lecture Notes in Physics Vol. 12 (Springer, Berlin, 1972), p. 103]. According to this theory the angular momentum is constant and equal to  $\frac{1}{2}$  only for  $\eta = \sqrt{2}/2$ . In our notation, the prediction is
- $$\frac{Ur}{\Omega a} = \frac{1}{4} \frac{1}{1-\eta^2} + \frac{1-2\eta^2}{2(1-\eta^4)} \left( (1-\eta) \frac{r-a}{b-a} + \eta \right)^2.$$
- This is in very close agreement with Smith and Townsend's measurements, but for our case the theory predicts a slightly negative slope while the observed slope in Fig. 5 is slightly positive. Unfortunately  $\eta = \sqrt{2}/2$  is too close to both our radius ratio and to Smith and Townsend's ( $\eta = 0.666$ ) to check Busse's theory.
- [14] Since the dissipation is higher in the boundary layer, Eq. (11) can be considered an upper limit for the core. A lower limit [about 45% of the value given by Eq. (11)] can be found by setting the dissipation equal to the turbulent production in energy budget.
- [15] H. Tennekes and J. L. Lumley, *A First Course in Turbulence* (MIT Press, Cambridge, MA, 1990).
- [16] Z.-S. She and E. Jackson, *Phys. Fluids A* **5**, 1526 (1993).
- [17] U. Frisch, *Turbulence* (Cambridge University Press, Cambridge, 1995).
- [18] A. N. Kolmogorov, *C. R. Acad. Sci. URSS* **30**, 9 (1941).
- [19] R. Benzi, S. Ciliberto, R. Tripiccone, C. Baudet, F. Massaioli, and S. Succi, *Phys. Rev. E* **48**, R29 (1993).
- [20] R. Benzi, S. Ciliberto, C. Baudet, G. Ruiz Chavarria, and R. Tripiccone, *Europhys. Lett.* **24**, 275 (1993).
- [21] G. Stolovitzky and K. R. Sreenivasan, *Phys. Rev. E* **48**, R33 (1993).
- [22] A. Arneodo *et al.*, *Europhys. Lett.* **34**, 411 (1996).
- [23] O. N. Boratav and R. B. Pelz, *Phys. Fluids* **9**, 1400 (1997).
- [24] F. Belin, P. Tabeling, and H. Willaime, *Physica D* **93**, 52 (1996).
- [25] G. Stolovitzky, K. R. Sreenivasan, and A. Juneja, *Phys. Rev. E* **48**, R3217 (1993).
- [26] F. Anselmet, Y. Gagne, E. J. Hopfinger, and R. A. Antonia, *J. Fluid Mech.* **140**, 63 (1984).
- [27] Z.-S. She and E. Léveque, *Phys. Rev. Lett.* **72**, 336 (1994).
- [28] S. Chen, K. R. Sreenivasan, M. Nelkin, and N. Cao, *Phys. Rev. Lett.* **79**, 2253 (1997).
- [29] C. R. Doering and P. Constantin, *Phys. Rev. Lett.* **69**, 1648 (1992).
- [30] P. Tabeling, G. Zocchi, F. Belin, J. Maurer, and H. Willaime, *Phys. Rev. E* **53**, 1613 (1996).